

Accurate polarization calibration of FAST spectral data for measurements of Zeeman splittings of OH megamasers in IRAS 02524+2046

L. G. Hou^{1,2,3,*}, X. Y. Gao^{1,2,3}, T. Hong^{1,2,3}, and J. L. Han^{1,2,3}

¹ National Astronomical Observatories, CAS, Jia-20 Datun Road, Chaoyang District, Beijing 100101, PR China

² School of Astronomy and Space Sciences, University of Chinese Academy of Sciences, Beijing 100049, China

³ State Key Laboratory of Radio Astronomy and Technology, Beijing 100101, China

Received 28 May 2025 / Accepted 10 February 2026

ABSTRACT

Context. An accurate polarization calibration is essential for a spectral data analysis and Zeeman splitting measurements. Two anomalies challenge our understanding of OH megamasers in IRAS 02524+2046: an unexplained 1667/1665 MHz flux-ratio deviation, and complex Stokes V signatures. Well-calibrated sensitive polarization observations are required to understand them.

Aims. We develop a polarization calibration solution for the L -band 19-beam receiver installed on the Five-hundred-meter aperture spherical radio telescope (FAST) to achieve a high calibration accuracy and thus enable accurate measurements of the OH megamaser properties in IRAS 02524+2046.

Methods. We determined the Mueller matrix solution for spectral observations across the 1050–1450 MHz frequency range with an accuracy of $\sim 0.01\%$ – 0.08% for circular polarization. We then applied it to FAST observational data of IRAS 02524+2046.

Results. Our results show narrower emission line components in the OH megamasers than previously reported, which are indistinguishable in the total power spectrum, but are detected in the circular polarization spectrum. The 1667 MHz OH megamaser emissions probably span a wide velocity range from $v_{\text{helio}} \sim 54\,750$ to $\sim 53\,580$ km s⁻¹, indicating greater complexity than previously recognized. Our fit of the total power and circular polarization spectra for IRAS 02524+2046 revealed ten line components with significant Zeeman splitting ($>3\sigma$), indicating in situ magnetic fields with a strength of approximately -24.5 mG to $+20.6$ mG, most of which (8/10) have positive values.

Key words. magnetic fields – masers – polarization – ISM: magnetic fields – galaxies: magnetic fields – galaxies: starburst

1. Introduction

An accurate polarization calibration is essential for analyzing spectral radio data. In general, the Mueller matrix for the entire observation system is determined through multiple observations of a standard polarization calibrator (e.g., 3C 286) at various parallactic angles (Heiles et al. 2001; Robishaw 2008; Robishaw & Heiles 2021; Ching et al. 2022, 2025). These polarization observations for an accurate calibration require significant telescope time.

The Five-hundred-meter aperture spherical radio telescope (FAST) is currently the world's largest single-dish radio telescope (Nan 2006). With its 300 m illuminated aperture and the sensitive L -band 19-beam receiver covering 1000–1500 MHz (Jiang et al. 2020), it possesses exceptional capabilities for observing pulsars (e.g., Han et al. 2021; Zhou et al. 2023b; Xu et al. 2022), fast radio bursts (e.g., Zhou et al. 2023a), radio continuum emission (e.g., Gao et al. 2022), and spectral lines (e.g., Hong et al. 2022; Hou et al. 2022). Since its commissioning in 2019, FAST has conducted multiple observations of polarization calibrators. A circular polarization calibration accuracy on the order of 10^{-4} for the central beam has been achieved by Ching et al. (2022). Based on observations of the calibrators 3C 286, 3C 48, and 3C 138, Ching et al. (2025) recently charac-

terized the temporal variations of the Mueller matrix elements for the polarization calibration for the 19 beams. An accurate calibration for all beams requires regular observations of polarization calibrators. The currently available observation data from FAST are insufficient for the purpose.

During spectral line observations, the calibration signals are routinely injected into the system in on-off mode for a rapid calibration. This approach enables us to determine gain and phase differences and variations between the receiver's two linearly polarized channels, as demonstrated in continuum polarization studies (e.g., Gao et al. 2022; Xiao et al. 2023) and pulsar polarization research (e.g., Wang et al. 2023, 2024). Since the commissioning of early scientific observations in 2019, FAST has accumulated a substantial volume of spectral line data using its L -band 19-beam receiver. The spectral backends record all four polarization products (XX , YY , $\text{Re}[X^*Y]$, and $\text{Im}[X^*Y]$) from the radio signals received through the two orthogonal linear polarizations X and Y .

We develop the procedures for accurately calibrating the full-polarization spectral data obtained by FAST. We then apply our approach to observations of OH megamasers in IRAS 02524+2046, which were observed in our projects to validate the data processing pipeline and Stokes V sign convention. The unprecedented sensitivity of FAST reveals new properties of OH megamasers in this galaxy. We briefly introduce the IRAS 02524+2046 and FAST observations in

* Corresponding author: lghou@nao.cas.cn

Section 2. The polarization calibration procedures are presented in Section 3. The new results for OH megamasers in IRAS 02524+2046 are presented in Section 4. Our discussions and conclusions are given in Section 5.

2. OH megamasers of IRAS 02524+2046 and FAST observations

The galaxy IRAS 02524+2046 is a starburst galaxy (Peng et al. 2020) and hosts luminous OH megamasers exhibiting unusual line ratios (Darling & Giovanelli 2002a; McBride et al. 2013). The OH spectrum of this galaxy presents broad-line components together with multiple strong and narrow components of the 1667 and 1665 MHz transitions. Some spectral components show day-to-day variation (Darling 2005, 2007). No satellite lines of the OH ground state near the rest frequency of 1612 MHz or 1720 MHz were detected (McBride et al. 2013). Observations with a high spatial resolution reveal that the compact maser emission line sources are distributed across a region of $\sim 210 \times 90$ pc (Peng et al. 2020; Wu et al. 2023).

There are two unresolved issues regarding the OH megamasers in IRAS 02524+2046. One issue is the anomalous flux ratio for the pair of the 1667 and 1665 MHz lines (Darling & Giovanelli 2002a; McBride et al. 2013), and the other issue is the complex features in the Stokes V spectrum (McBride & Heiles 2013). The high-velocity feature at $v_{\text{helio}} \sim 54\,725$ km s $^{-1}$, attributed to the OH 1665 MHz transition in previous studies (Darling & Giovanelli 2002a; McBride et al. 2013; Peng et al. 2020), shows an unusually strong integrated flux density compared to the 1667 MHz line at a heliocentric velocity $v_{\text{helio}} \sim 54\,300$ km s $^{-1}$. Unless otherwise specified, the v_{helio} of the observed spectrum throughout this work was calculated using the rest frequency $\nu_0 = 1667.3590$ MHz. The line ratio $R_H = F_{1667}/F_{1665}$, where F_ν represents the integrated flux density across each emission line, is about 1.3 (McBride et al. 2013) or 1.4 (Darling & Giovanelli 2002a), which is in the range of thermal emission values of 1.0–1.8. It presents a challenge to the pumping model of OH megamasers (Lockett & Elitzur 2008), which predicts that the 1667 MHz line dominates the 1665 MHz line for line widths exceeding ~ 2 km s $^{-1}$, as commonly seen in OH megamasers. Even after multi-Gaussian decomposition, both lines of the pair of 1667 and 1665 MHz transitions maintain significantly broader line widths (>2 km s $^{-1}$). On the other hand, it is difficult to fit the Stokes V spectrum features (McBride & Heiles 2013) to demonstrate the Zeeman splitting and derive the magnetic fields of OH megamasers, because significant residuals with prominent peaks and dips persist in all fitting attempts.

IRAS 02524+2046 was observed by FAST during two observation sessions (see below) using the central beam of the L -band 19-beam receiver with a zenith angle from approximately 24.7° to 9.4° and a small system temperature change in a range of about $T_{\text{sys}} \sim 23$ K to 20 K (Jiang et al. 2020). The two linear polarization signals X and Y were extracted by an orthomode transducer for each of the 19 beams, making this system particularly well suited for precise measurements of circular polarization signals (Heiles et al. 2001) (see Table 1).

The first observation was carried out on 11 August 2023 using the central beam of the L -band 19-beam receiver. The TrackingWithAngle mode was adopted to track the target for approximately one hour, with a pointing accuracy of about $8''$ (Jiang et al. 2020), a main-beam efficiency of ~ 0.63 , and a half-power beam width of $\sim 2.8'$ (Jiang et al. 2020) or $\sim 2.9'$ (Chen et al. 2025) at 1420 MHz. During the observations, the

receiver continuously rotates to compensate for the real-time field rotation. Additionally, the feed angle can be preset to any value between -80° and $+80^\circ$. We maintained the default 0° setting of the feed angle for these observations. A calibration signal from a low-noise diode with an amplitude of about 1.1 K (Jiang et al. 2020) was periodically injected for 1 s every 16 s, which can be used to calibrate the temperature scale and the polarization performance of the system (Sun et al. 2021). The polarization signals were recorded across 1024 K channels covering the observing frequencies from 1000 MHz to 1500 MHz, corresponding to a frequency resolution of 0.477 kHz (equivalent to 0.10 km s $^{-1}$ velocity resolution at the 1420 MHz HI line).

The second observation was conducted on 12 August 2023 using identical instrument settings, but with the feed angle fixed at 45° after compensating for the field rotation to examine potential polarization side-lobe effects. We note that IRAS 02524+2046 is located at Galactic coordinates $(l, b) = (158.0^\circ, -33.3^\circ)$. The spectral line data of the foreground Galactic HI are recorded simultaneously, which provides an independent assessment of the polarization calibration quality, as discussed in subsequent sections.

For the polarization calibration, we obtained five drift-scan observations of the standard calibrator 3C 286 on 19 August 2023 at different rotation angles of -60° , -30° , 0° , $+30^\circ$, and $+60^\circ$ (e.g., Jiang et al. 2020; Ching et al. 2022, 2025). Given the strong flux density of 3C 286, we employed a high noise diode with an amplitude of about 12.5 K (Jiang et al. 2020) that injected calibration signals in a period of 1 s during the drift scans, with spectral data recorded every 0.5 s. Additionally, we incorporated FAST observations of 3C 286 on 7 and 14 August 2023 using the multi-beam calibration mode during the scheduled maintenance periods to calibrate the flux density.

3. Calibration of polarized spectral data

Based on the intensities of periodically injected reference signals, the four polarization products (XX , YY , $\text{Re}[X^*Y]$, and $\text{Im}[X^*Y]$) were first calibrated to the scale of the antenna temperature T_A and were then converted into the heliocentric frame by correcting for the Doppler effect. The radio frequency interference (RFI) in the data was inspected and removed as done by Hou et al. (2022). Afterward, the observed Stokes parameters were derived from the four polarization products using

$$\begin{bmatrix} I_{\text{obs}} \\ Q_{\text{obs}} \\ U_{\text{obs}} \\ V_{\text{obs}} \end{bmatrix} = \begin{bmatrix} XX + YY \\ XX - YY \\ 2\text{Re}[X^*Y] \\ \pm 2\text{Im}[X^*Y] \end{bmatrix}, \quad (1)$$

where the sign ambiguities in the polarization signals caused by internal cable connections were solved by comparing our results with published values. Following Robishaw et al. (2008) and McBride & Heiles (2013), we adopted the IAU definitions of Stokes $V = \text{RCP} - \text{LCP}$, in accordance with the IEEE standard that the right circular polarization (RCP) rotates clockwise as viewed from the radio source, and the left circular polarization (LCP) rotates counterclockwise.

The observed Stokes parameters (I_{obs} , Q_{obs} , U_{obs} , and V_{obs}) are the products of the radio source polarization signals modified by the receiving system of a telescope, as

$$\begin{bmatrix} I_{\text{obs}} \\ Q_{\text{obs}} \\ U_{\text{obs}} \\ V_{\text{obs}} \end{bmatrix} = M_{\text{tot}} \cdot \begin{bmatrix} I'_{\text{source}} \\ Q'_{\text{source}} \\ U'_{\text{source}} \\ V'_{\text{source}} \end{bmatrix}. \quad (2)$$

Table 1. OH megamaser observation parameters for IRAS 02524+2046.

Observation date	11 and 12, August 2023
Observed frequency range	1000–1500 MHz
Effective frequency range	1050–1450 MHz
Beam size	~2.8'–2.9' @ 1420 MHz
Polarization products	XX, YY, Re[X*Y], Im[X*Y]
Channel number	1024 K
Sampling time	0.5 s
Integration time	110 minutes
Redshift of IRAS 02524+2046	0.1814 ± 0.0002 [†]
Rest frequencies of the four OH lines [‡]	1612.2310, 1665.4018, 1667.3590, 1720.5300 MHz
Observed frequencies*	1364.6783, 1409.6850, 1411.3416, 1456.3484 MHz

Notes. [†]Redshift derived from optical spectrophotometry (Darling & Giovanelli 2006). [‡]Rest frequencies of the four OH transitions were taken from <https://pml.nist.gov/cgi-bin/micro/table5/start.pl>. *Observed frequencies were calculated using their rest frequencies and the galaxy redshift.

Here, M_{tot} is the polarization transfer function of the receiving system (Heiles et al. 2001), which we discuss below. The polarized source signals are modified by the parallactic angle, θ , via

$$\begin{bmatrix} I'_{\text{source}} \\ Q'_{\text{source}} \\ U'_{\text{source}} \\ V'_{\text{source}} \end{bmatrix} = \begin{bmatrix} 1 & 0 & 0 & 0 \\ 0 & \cos 2\theta & \sin 2\theta & 0 \\ 0 & -\sin 2\theta & \cos 2\theta & 0 \\ 0 & 0 & 0 & 1 \end{bmatrix} \cdot \begin{bmatrix} I_{\text{source}} \\ Q_{\text{source}} \\ U_{\text{source}} \\ V_{\text{source}} \end{bmatrix}. \quad (3)$$

For FAST observations, the feed is always rotated to compensate for field rotation, so this modification is usually not present as θ was set to 0°. To derive intrinsic source properties from the observed Stokes parameters, the polarization transfer function of the receiving system (Heiles et al. 2001), M_{tot} , has to be solved, which can be expressed as

$$\begin{bmatrix} 1 & X_{I2Q} & X_{I2U} & 2\epsilon \sin \phi \\ \Delta G/2 & X_{Q2Q} & X_{Q2U} & \Delta G \epsilon \sin \phi \\ 2\epsilon \cos(\phi + \psi) & -\sin 2\alpha \cos \psi & \cos 2\alpha \cos \psi & -\sin \psi \\ 2\epsilon \sin(\phi + \psi) & -\sin 2\alpha \sin \psi & \cos 2\alpha \sin \psi & \cos \psi \end{bmatrix}$$

for the dual linear feeds of the FAST L -band 19-beam receiver (Ching et al. 2025). Here, ϵ denotes the imperfection of the feed in producing nonorthogonal polarizations, ϕ is the phase angle at which the voltage coupling ϵ occurs, α measures the voltage ratio of the polarization ellipse produced when observing a pure linear polarization signal, ΔG indicates the error in the relative intensity calibration of the two polarization channels, and ψ is the phase difference between the reference noise signal and the incoming radiation from the sky, $X_{I2Q} = -2\epsilon \cos \phi \sin 2\alpha + \frac{\Delta G}{2} \cos 2\alpha$, $X_{I2U} = 2\epsilon \cos \phi \cos 2\alpha + \frac{\Delta G}{2} \sin 2\alpha$, $X_{Q2Q} = -\Delta G \epsilon \cos \phi \sin 2\alpha + \cos 2\alpha$, and $X_{Q2U} = \Delta G \epsilon \cos \phi \cos 2\alpha + \sin 2\alpha$. To determine the intrinsic source properties from the observed Stokes parameters, we investigated two different calibration approaches.

3.1. Polarization calibration resting on injected reference signals

Polarization calibration using the injected reference signals has been successfully applied to various FAST observations, including studies of radio continuum sources and pulsars (e.g., Sun et al. 2021; Wang et al. 2023). Instead of determining all Mueller matrix elements (e.g., Heiles et al. 2001; Robishaw 2008; Robishaw & Heiles 2021), this simplified

approach focuses on solving for the two dominant parameters, ΔG and ψ , which account for the mismatch between the amplitudes and phases of the gains of the two orthogonal linear feeds, respectively. This method offers two key advantages. One advantage is that no additional observations of the polarization calibrator are needed, which saves time. The other advantage is that the time-dependent small variation in the system polarization characteristics, even during the observations, can be monitored and corrected.

Following the method of Sun et al. (2021), we determined ΔG and ψ for each frequency channel and applied these corrections to the five 3C 286 drift scans obtained at different rotation angles. We measured a linear polarization fraction $P_{\text{src}} = \sqrt{Q^2 + U^2}/I = 9.3\% \pm 0.5\%$ and polarization angle $\chi = \frac{1}{2} \arctan \frac{U}{Q} = 25.5^\circ \pm 0.8^\circ$ at 1400 MHz after ionospheric correction using the ionFR package (Sotomayor-Beltran et al. 2013). These results are roughly consistent with reference values of $P_{\text{src}} = 9.90\% \pm 0.003\%$ (Taylor & Legodi 2024) and $\chi \sim 27.8^\circ$ – 28.6° at 1400 MHz (Taylor & Legodi 2024) and with our results in Sect. 3.2. According to Ching et al. (2025), the calibrated polarization percentages and polarization angles of 3C 286 measured by FAST at 1420 MHz show P_{src} values ranging from ~9.3% to 9.8% during 2019 to early 2023, with χ values varying between ~28° and 32°. However, the calibrated V/I values deviate from zero across 1050–1450 MHz, ranging from about -0.5% to +0.4%. The absolute median and mean values are $0.15\% \pm 0.01\%$ and $0.17\% \pm 0.01\%$, respectively, indicating that the calibrated V by this method is dominated by the uncompensated leakage of I at the 0.2% level.

To assess the reliability of this simple calibration method, we examined the calibrated spectra of IRAS 02524+2046 around the Galactic HI 21 cm line region. For this target direction, circular polarization of the Galactic HI 21 cm line is expected to be undetectable given our observational integration time. The upper panels of Fig. 1 show that the calibrated V spectrum has a very similar shape as the I profiles near the heliocentric velocity of -10 km s^{-1} , indicating that V has been dominated by the uncompensated leakage of I into V at approximately -0.2% near 1420.4 MHz. For most of the spectra data accumulated by FAST in the past few years, when observational data for determining the full Mueller matrix are lacking and the simple calibration method based on the injected reference signals is applied, the uncompensated leakage of I into V at the ~0.2% level cannot be corrected.

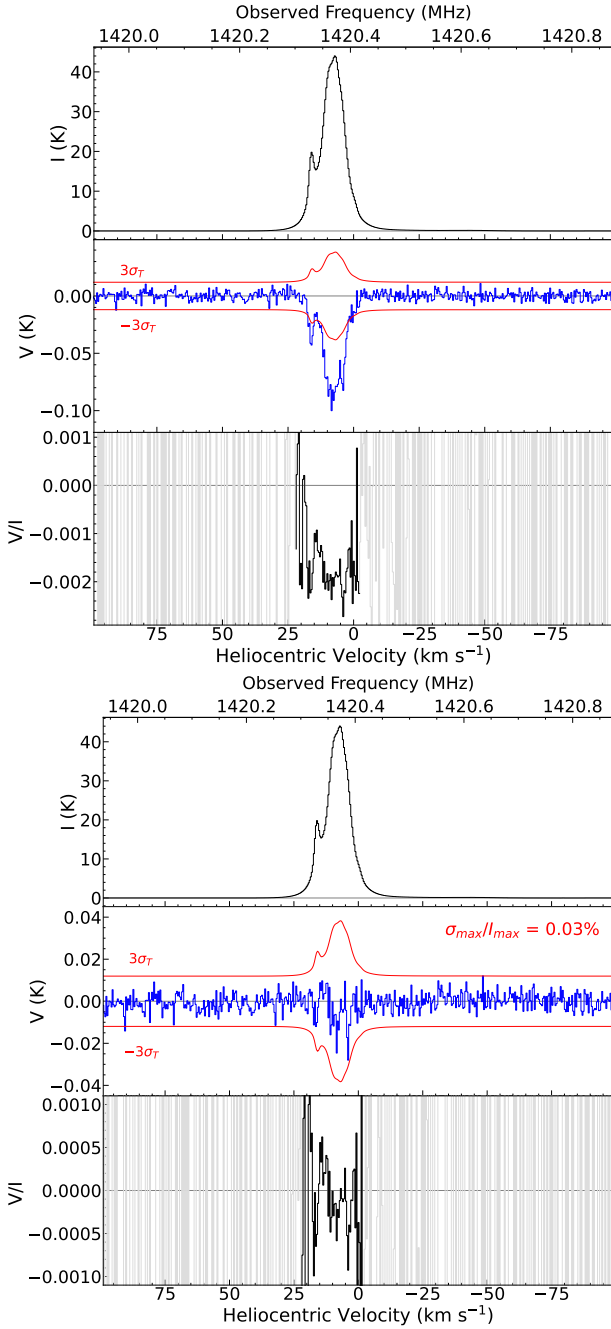


Fig. 1. Calibrated results of the Galactic HI 21 cm lines using the two approaches described in Sects. 3.1 and 3.2. These FAST observations targeted IRAS 02524+2046 at Galactic coordinates $(l, b) = (158.0^\circ, -33.3^\circ)$, with a total integration time of 110 minutes. The *upper panels* demonstrate that the quick calibration method using injected reference signals achieves polarization measurement accuracy of $\sim 0.2\%$. The σ_T lines are derived by considering the contributions from HI emission features following the method of Jing et al. (2023). The *lower panels* show results after a full Mueller matrix solution and leakage correction, reaching a higher calibration accuracy of $\sim 0.03\%$.

3.2. Polarization calibration based on observations of 3C 286

The standard polarization calibrator 3C 286 was used to determine the Mueller matrix coefficients for the FAST telescope system. In general, the intrinsic circular polarization V of 3C 286 is assumed to be zero at L -band, as confirmed by recent observations (e.g., Taylor & Legodi 2024). To derive the Mueller

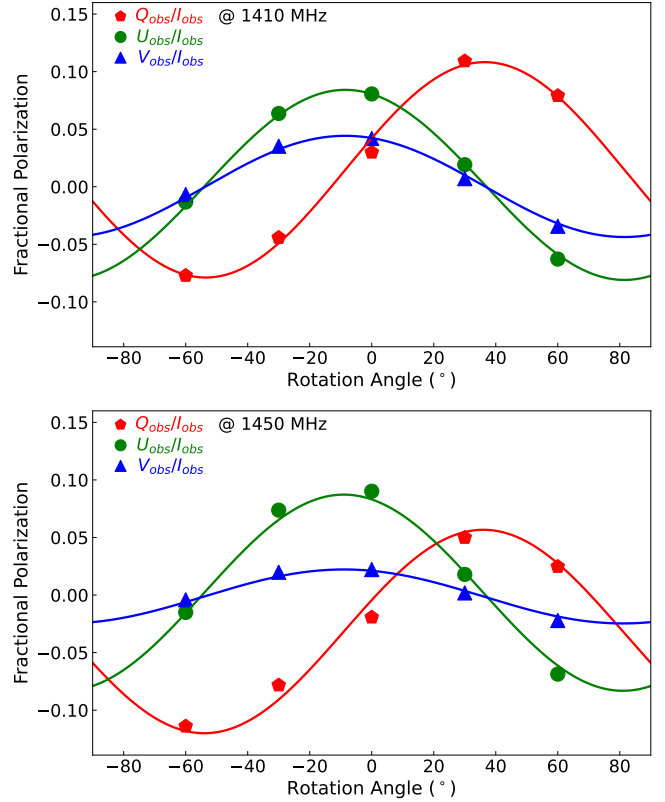


Fig. 2. Fitting the observed fractional polarizations in two example frequency channels of 1410 MHz (*upper*) and 1450 MHz (*lower*) to derive the Mueller matrix elements. The different symbols indicate different observed fractional polarization components, as shown in the plots. The solid curves show the fitting results. The data were obtained from FAST observations on 19 August 2023.

matrix from FAST's five 3C 286 drift scans, we implemented the method of Heiles et al. (2001), and we refer to the documentation for the package Robshaw/Heiles SToKes (RHSTK)¹ as well as the procedures described in Ching et al. (2025). We fit the observed fractional polarizations ($Q_{\text{obs}}/I_{\text{obs}}$, $U_{\text{obs}}/I_{\text{obs}}$, and $V_{\text{obs}}/I_{\text{obs}}$) for each frequency channel. The fitting results for two frequency channels are shown in Fig. 2. Across the frequency ranges of 1050–1150 MHz and 1300–1450 MHz, the fit parameters vary as follows: ΔG , -3.0% to 2.9% ; ψ , -0.8° to 1.4° ; ϵ , -0.38% to 0.29% ; ϕ , 16° to 177° ; and α , -0.3° to -0.2° (see Fig. A.1). The Mueller matrix parameters for the 1150–1300 MHz range were not determined due to severe RFI. The derived Mueller matrix was then applied to observational data to obtain corrected Stokes parameters (I , Q , U , V). The sign of Stokes V was verified using previously known results of OH megamasers from IRAS 02524+2046 (McBride & Heiles 2013).

Following standard calibration, we measured a linear polarization fraction $P_{\text{src}} = 9.6\% \pm 0.3\%$ at 1400 MHz for 3C 286, consistent with the value $9.90\% \pm 0.003\%$ given by Taylor & Legodi (2024) and the results of $\sim 9.3\%$ to 9.8% reported by Ching et al. (2025), and we obtained the polarization angle $\chi = 36.4^\circ \pm 0.8^\circ$. We calculated the Faraday rotation due to Earth's ionosphere with the package ionFR (Sotomayor-Beltran et al. 2013), and we then corrected the polarization angle to $27.2^\circ \pm 0.9^\circ$ at 1400 MHz, consistent with the intrinsic polarization angle range of about 27.8° – 28.6° at 1400 MHz given in Fig. 2 of Taylor & Legodi (2024). This

¹ <https://w.astro.berkeley.edu/%7Eheiles>

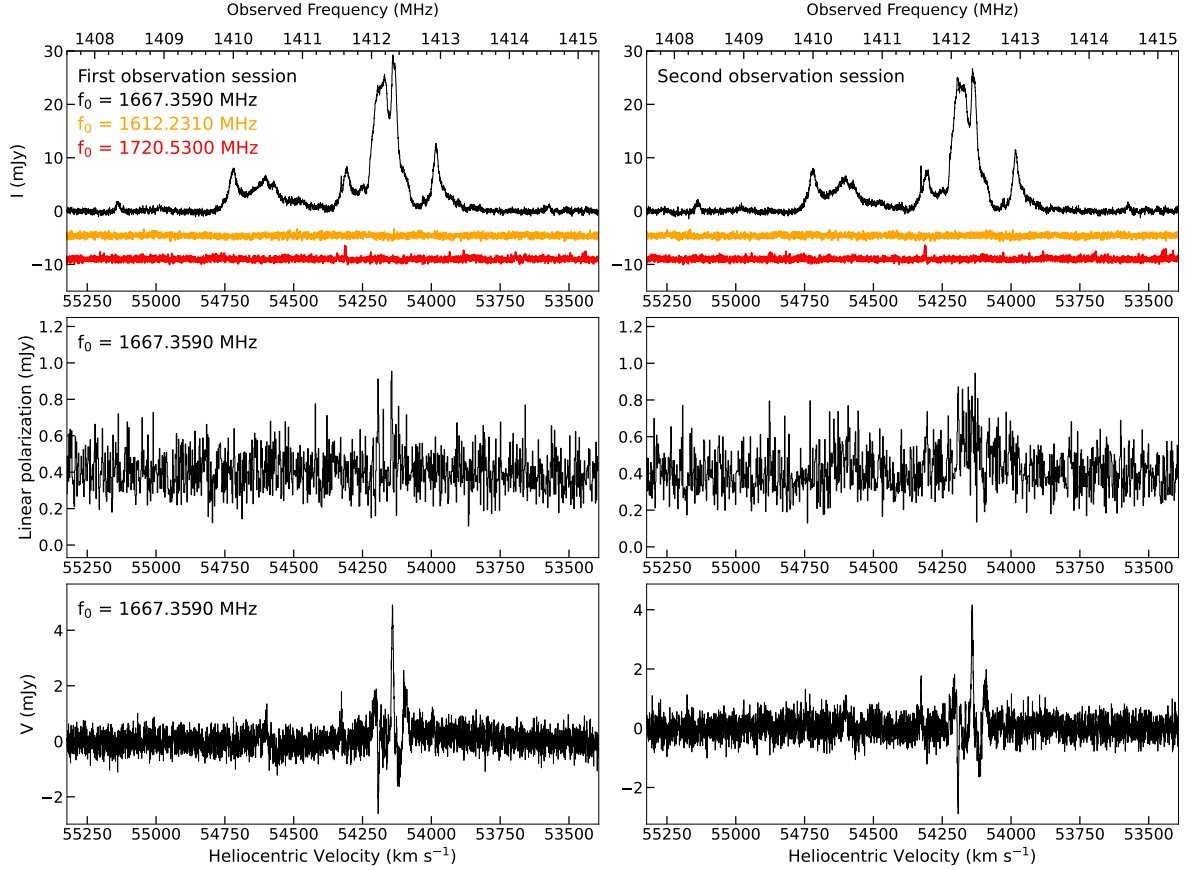


Fig. 3. OH megamaser emission from IRAS 02524+2046 observed by FAST during two observation sessions. *Top panels:* Stokes I spectra aligned by heliocentric velocity for the OH ground-state transitions. The vertical offsets are applied for clarity. *Middle panels:* Linear polarization spectra for the 1665 MHz and 1667 MHz OH megamaser lines. *Bottom panels:* Circular polarization spectra for both OH transitions.

generally agrees with the χ values of $\sim 28^\circ$ to 32° at 1420 MHz given by Ching et al. (2025). Across our observed frequency range, the calibrated V/I values are around zero, with absolute median and mean values of $0.03\% \pm 0.01\%$ and $0.06\% \pm 0.01\%$, respectively. We understand that the circular polarization of 3C 286 should be zero at L band (e.g., Taylor & Legodi 2024), and any residuals should reflect the uncorrected leakage from I to V (i.e., $\alpha_v I_v$) in the calibration procedure above. This interpretation is supported by our subsequent analysis of Galactic HI 21 cm line observations. We then further repaired the leakage terms $\alpha_v I_v$ by adding them to the calibrated V spectrum, and we achieved a final circular polarization accuracy of about 0.01% – 0.08% across 1050–1450 MHz.

To verify our calibration results, we analyzed Galactic HI 21 cm line observations toward IRAS 02524+2046 ($l = 158.0^\circ$, $b = -33.3^\circ$) obtained with FAST during a 110-minute on-source integration. After the baseline and standing waves were discounted (see Jing et al. 2023, and Appendix B for examples), we derived the Stokes I , V and fractional polarization V/I for the HI 21 cm lines as shown in the lower panels of Fig. 1. The fractional polarization V/I ranges from about -0.06% to 0.06% across the line emission regions. No similar shape of V to the I profiles implies that the uncompensated leakage of I into V , if it exists, will be lower than 0.03% near 1420.4 MHz. These results demonstrate FAST’s capability to measure weak circular polarization with high precision. The consistent V/I levels between calibrated 3C 286 observations and the calibrated Galactic HI 21 cm line observations suggest that the Mueller matrix values for FAST’s central

beam probably do not change significantly over timescales of weeks.

For timescales ranging from months to years, the Mueller matrix of FAST’s 19-beam receiver central beam varies in time, as reported by Ching et al. (2025). When applying average Mueller matrix parameters to FAST observations from 2020–2022, fractional circular polarization measurements exceeding 1.5% can be considered reliable detections (Ching et al. 2025). This performance is comparable to the reference-signal calibration method described in Sect. 3.1. These findings, together with our results, highlight the importance of regular calibrator observations for maintaining polarization calibration accuracy.

4. The features of OH megamasers in IRAS 02524+2046 observed by FAST

We applied the Mueller matrix calibration to the IRAS 02524+2046 spectral data and obtained similar results from two independent FAST observations, as shown in Fig. 3. The one-day variation is apparent in some components (Fig. 4). After combining the two datasets, we derived the Stokes I and V spectra of the OH megamasers, as shown in Fig. 5. Because the total on-source integration time is about 110 minutes by the super-sensitive FAST, we obtained the fine spectrum in Fig. 5 with a root mean square (RMS) noise of only about 0.3 mJy per channel at 0.48 km s^{-1} velocity resolution. Key findings include the detection of detailed OH megamaser features from IRAS 02524+2046 and a high circular polarization reaching up

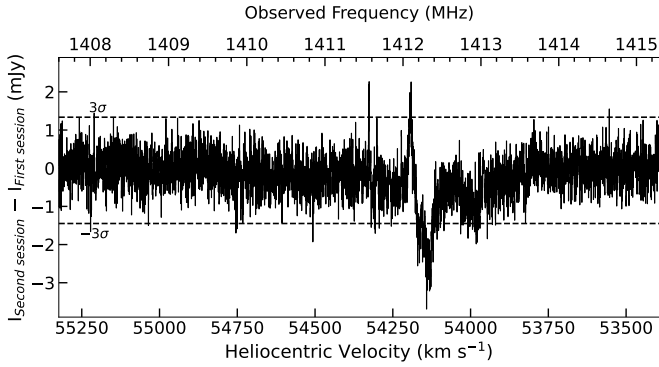


Fig. 4. Difference in the Stokes I spectrum between two observation sessions, indicating the one-day variation in the spectral lines.

to $\sim 16\%$ at certain frequencies. As we inspected the raw data in detail, these OH megamaser features detected by FAST are not caused by radio frequency interference.

4.1. The new features of OH megamaser lines

The top panel of Fig. 5 shows the observed Stokes I spectrum against the heliocentric velocity for the two main line transitions of the OH ground state at rest frequencies of 1665.4018 MHz and 1667.3590 MHz and the two satellite lines at the rest frequencies of 1612.2310 MHz and 1720.5300 MHz. The 1612 MHz spectrum shows no detectable features, and the RMS level of ~ 0.3 mJy demonstrates FAST’s exceptional sensitivity. A very narrow emission line feature in the 1720 MHz spectrum was detected with a peak flux density of 2.4 ± 0.1 mJy, a line center $54\,312.0 \pm 0.1$ km s $^{-1}$ in the heliocentric frame, and a full width at half maximum (FWHM) line width 4.6 ± 0.3 km s $^{-1}$. This feature appears in the two independent FAST observation sessions (see Fig. 3). The line width is smaller than the typical 10 km s $^{-1}$ width of OH megamaser components (Lockett & Elitzur 2008). To date, OH satellite lines in the L band have only been detected in seven galaxies: Arp 220 (Baan & Haschick 1987; McBride et al. 2013), III ZW 35 (Baan et al. 1989; McBride et al. 2013), IRAS 17207–0014 (Baan et al. 1989; McBride et al. 2013), Arp 299 (IC 694) and Mrk 231 (Baan et al. 1992), IRAS 10173+0829, and IRAS 15107+0724 (McBride et al. 2013).

The dominant 1665 MHz and 1667 MHz OH megamaser features appear within $v_{\text{helio}} \sim 53\,800$ – $54\,850$ km s $^{-1}$, consistent with previous single-dish (Darling & Giovanelli 2002a; McBride et al. 2013; Wu et al. 2023) and interferometry (Peng et al. 2020) observations. However, significant flux density discrepancies exist among different studies. When we take the strongest feature near $v_{\text{helio}} \sim 54\,150$ km s $^{-1}$ as an example, the flux density values given by different works are ~ 28 mJy (this work), ~ 30 mJy (Wu et al. 2023), ~ 80 mJy (McBride et al. 2013), and ~ 40 mJy (Darling & Giovanelli 2002a). The OH megamaser variability likely contributes to these differences. This variability was first discovered by Darling & Giovanelli (2002b) and is commonly interpreted as a result of interstellar scintillation (e.g., Darling & Giovanelli 2002b; Wu et al. 2023), although not all of the components present apparent variation. Intrinsic changes in the physical conditions of the maser environment (McBride et al. 2015; Harvey-Smith et al. 2016) might also account for the variability. For IRAS 02524+2046, the strong variability of OH megamasers across multiple spec-

tral components has been documented by Arecibo observations. Notably, the RMS spectrum reveals significant day-to-day variations (Darling 2005, 2007). The short-term variability is also evident in our data. As shown in Fig. 4, day-to-day changes are noticeable in some emission components centered from $v_{\text{helio}} \sim 54\,000$ km s $^{-1}$ to $54\,250$ km s $^{-1}$.

In comparison to previous works, the FAST spectrum presents more detailed emission line features resting on its high sensitivity and high spectral resolution. For instance, a prominent narrow emission line component from the 1667 MHz transition appears near $v_{\text{helio}} \sim 54\,327$ km s $^{-1}$, which has a peak flux density of 3.9 ± 0.2 mJy, a line center of $54\,326.96 \pm 0.06$ km s $^{-1}$, and a FWHM line width of 2.6 ± 0.2 km s $^{-1}$. The line width is narrower than that of typical OH megamaser components (10 km s $^{-1}$, Lockett & Elitzur 2008) and is broader than Galactic star-forming region OH masers ($\lesssim 1$ km s $^{-1}$, e.g., Caswell et al. 2013, 2014). This narrow component is unlikely to originate from RFI, as it was consistently detected across multiple independent observational datasets: in both sessions of our FAST observations, and in the separate observations conducted by Darling & Giovanelli (2002a) and McBride & Heiles (2013) with Arecibo. Outside this velocity range, there are two emission line features. One feature is a new $\sim 3\sigma$ detection at $v_{\text{helio}} \sim 53\,580$ km s $^{-1}$, most likely from 1667 MHz OH lines considering its observed frequency. The other is a $>5\sigma$ feature at $v_{\text{helio}} \sim 55\,140$ km s $^{-1}$, which was previously reported by Darling & Giovanelli (2002a, see the upper right panel of their Fig. 1), and which corresponds to a heliocentric velocity of $\sim 54\,725$ km s $^{-1}$ for 1665 MHz OH transition.

The detection of the 1665 MHz line near the heliocentric velocity of $\sim 54\,725$ km s $^{-1}$ provides crucial insight into the unusual flux ratio of the pair of 1667 MHz and 1665 MHz lines previously reported (Darling & Giovanelli 2002a; McBride et al. 2013). In the Arecibo survey results for 50 OH megamaser galaxies, all the identified 1665 MHz OH megamaser lines showed much stronger 1667 MHz counterparts (Darling & Giovanelli 2000, 2001, 2002a). As shown by the blue spectrum in Fig. 5, the weak feature far left near $v_{\text{helio}} \sim 55\,140$ km s $^{-1}$ in the black spectrum should be attributed to the 1665 MHz transition at the heliocentric velocity $\sim 54\,725$ km s $^{-1}$, where a much stronger emission line component appears in the black spectrum. The emission line component near $v_{\text{helio}} \sim 54\,725$ km s $^{-1}$ in the black spectrum should not be simply attributed to the 1665 MHz OH megamasers alone, as done by e.g., Darling & Giovanelli (2002a), McBride et al. (2013), and Peng et al. (2020), but is likely to be blended emission from the 1667 MHz and 1665 MHz transitions. We adopted a median R_H value of 5.9 and a typical interquartile range of 3.2–8.4 from the OH megamaser sample of Darling & Giovanelli (2002c). Using this typical R_H value and the integrated intensity of the 1665 MHz megamasers at $v_{\text{helio}} \sim 55\,140$ km s $^{-1}$, we estimated the contribution of the 1667 MHz line to the emission at $v_{\text{helio}} \sim 54\,725$ km s $^{-1}$. This allowed us to subsequently estimate an R_H value of $2.4^{+2.8}_{-0.9}$ for the emissions near $v_{\text{helio}} \sim 54\,300$ km s $^{-1}$. Consequently, the previously reported anomalous line ratio near $v_{\text{helio}} \sim 54\,300$ km s $^{-1}$ can be naturally explained by the blending of both lines at the same velocities. Therefore, the intensity ratio of the 1665 MHz to 1667 MHz transitions, shown in the upper middle panel of Fig. 5, is likely overestimated near $v_{\text{helio}} \sim 54\,300$ km s $^{-1}$ and underestimated near $v_{\text{helio}} \sim 54\,725$ km s $^{-1}$. A potential overestimation may also exist near $v_{\text{helio}} \sim 54\,050$ km s $^{-1}$, although the individual maser lines are difficult to distinguish in this region. Our results suggest that the 1667 MHz OH megamaser emission

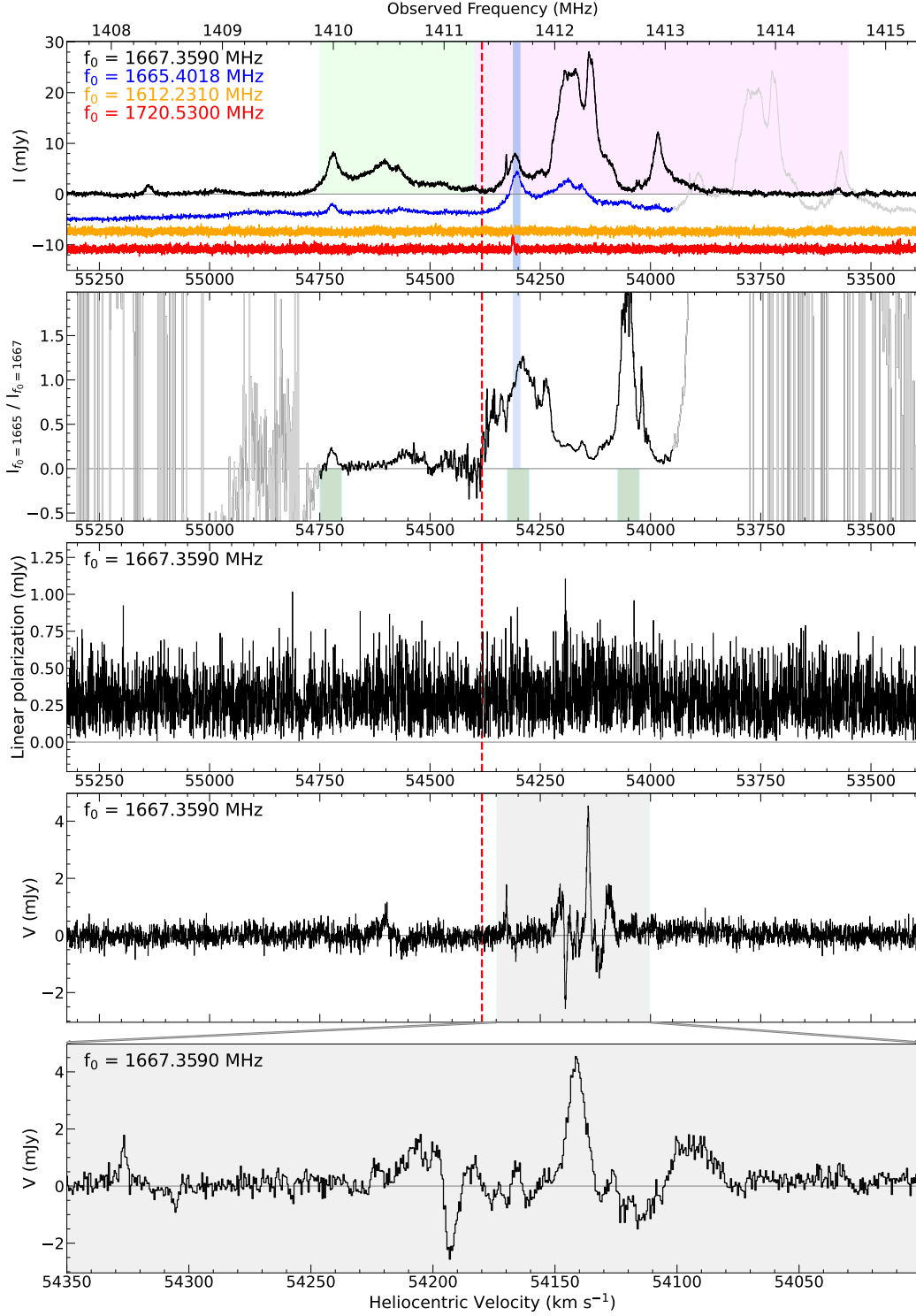


Fig. 5. OH megamaser emissions from IRAS 02524+2046 observed by FAST for 110 minutes. *Top panel:* Stokes I spectra of the OH ground state aligned by heliocentric velocity, with given vertical offsets for clarity. The dashed vertical line marks the heliocentric velocity $v_{\text{helio}} = cz = 54382 \text{ km s}^{-1}$ of IRAS 02524+2046 for a redshift $z = 0.1814$ from optical spectrophotometry (Darling & Giovanelli 2006). The thick light blue line highlights the pair of 1667 and 1665 MHz OH megamaser lines, showing an unusual flux ratio reported by Darling & Giovanelli (2002a) and McBride et al. (2013). The fuchsia shaded area indicates the probable velocity range of the 1667 MHz OH megamaser emission lines, while the lime shaded area represents the velocity range in which the 1665 and 1667 MHz lines are likely mixed (see Sect. 4.1). *Upper middle panel:* Intensity ratio of the 1665 MHz to 1667 MHz lines. The dark green shaded areas indicate that the intensity ratio of the 1665 MHz to 1667 MHz transitions is potentially overestimated near $v_{\text{helio}} \sim 54050 \text{ km s}^{-1}$ and $v_{\text{helio}} \sim 54300 \text{ km s}^{-1}$, and underestimated near $v_{\text{helio}} \sim 54725 \text{ km s}^{-1}$. *Middle panel:* Linear polarization spectrum at the heliocentric velocity for 1667.3590 MHz line. *Lower middle panel:* Stokes V spectrum at the heliocentric velocity for 1667.3590 MHz line, showing some features from the 1665.4018 MHz transition. *Bottom panel:* Zoomed-in view of the Stokes V spectral features.

from IRAS 02524+2046 extends beyond $v_{\text{helio}} \sim 54\,400 \text{ km s}^{-1}$, with significant components at higher velocities, as shown in Fig. 5. Additionally, we note that the new interpretation reveals that the 1667 MHz OH megamaser emissions are distributed on either side of the systemic velocity of IRAS 02524+2046 ($v_{\text{helio}} = 54\,382 \text{ km s}^{-1}$, determined from optical spectrophotometry, Darling & Giovanelli 2006). This differs from previous results, which suggested emissions on only one side (e.g., Darling & Giovanelli 2002a; McBride et al. 2013).

The linear polarization spectrum of the 1665 MHz and 1667 MHz OH megamasers is shown in the middle panel of Fig. 5. We detect a polarization feature with $\sim 3.6\sigma$ significance at $v_{\text{helio}} \sim 54\,190 \text{ km s}^{-1}$. This feature has a polarized intensity of $\sim 0.54 \text{ mJy}$ compared to the total intensity peak of $\sim 24 \text{ mJy}$ at the same velocity, corresponding to a linear polarization degree of $\sim 2.3\%$. The origin of the linear polarization observed in the OH megamasers remains unclear. An instrumental leakage of Stokes I to Q and/or U is unlikely, as the intense OH emission features around $v_{\text{helio}} \sim 54\,150 \text{ km s}^{-1}$ in the I spectrum would otherwise also imprint a detectable signature on the linear polarization spectrum. Instead, we speculate that the linear polarization might originate from a π component, a phenomenon detected in approximately 16% of Galactic OH masers, including ground-state and excited-state transitions (Green et al. 2015). No other polarization features with a significance above 3σ are present in the linear polarization spectrum.

The Stokes V spectrum for the main OH ground-state transitions is shown in the lower two panels of Fig. 5. In addition to the three prominent features discussed by McBride et al. (2013), our FAST observations reveal new spectral components that appear as peaks and dips within the velocity range $v_{\text{helio}} \sim 54\,070\text{--}54\,350 \text{ km s}^{-1}$. While Zeeman splitting remains the primary mechanism for Stokes V features in OH masers, non-Zeeman effects might contribute as well. Theoretical studies indicated that the linear-to-elliptical polarization conversion and Faraday rotation in maser-emitting clouds can produce antisymmetric V profiles, which particularly affect weakly split interstellar masers of SiO, H₂O, and CH₃OH (Watson 2009). For OH masers in star-forming regions, observed V profiles typically reflect Zeeman splitting, but might be modified by magnetic field gradients, velocity gradients, and radiative transfer effects (e.g., Nedoluha & Watson 1990). The situation becomes more complex for OH megamasers, where line couplings between Doppler-shifted transitions (e.g., the 1665 MHz and 1667 MHz lines) in the velocity gradient conditions of gas clouds might additionally affect the V profiles, although the observed V profiles of OH megamasers are also thought to be Zeeman dominated (Robishaw et al. 2008; McBride & Heiles 2013). Following established methods (Robishaw et al. 2008; McBride & Heiles 2013), we analyzed the observed Stokes I and V spectra to extract magnetic field information.

4.2. The Zeeman splittings of OH megamaser lines

Following Robishaw et al. (2008) and McBride & Heiles (2013), we assumed that the Zeeman splitting of every OH megamaser component is smaller than the line width. The V spectrum can then be expressed as

$$V = \sum_{i=1}^n \left(\frac{\nu}{\nu_{0i}} \right) \left(\frac{dI_i}{d\nu} \right) \frac{b_i}{2} B_{//i} + C_{I2V}, \quad (4)$$

where ν is the observing frequency, ν_{0i} is the rest frequency of the OH transition for the i th OH megamaser line com-

ponent, ν/ν_{0i} accounts for the frequency compression of the redshifted line, I_i is the total intensity profile of the i th OH megamaser component, b_i is the splitting coefficient, which is $1.964 \text{ Hz } \mu\text{G}^{-1}$ for the 1667.3590 MHz line and $3.270 \text{ Hz } \mu\text{G}^{-1}$ for the 1665.4018 MHz line (Heiles et al. 1993; Robishaw 2008), and $B_{//i}$ is the strength of the line-of-sight magnetic field with a positive value for magnetic fields pointing away from the observer. The parameter C_{I2V} was originally used to quantify the uncompensated leakage from Stokes I to V . However, in our analysis, the fitted C_{I2V} represents a composite signal, which includes both the genuine uncompensated I -to- V leakage and residual standing wave contamination. This is because residual components persist despite the modeling and subtraction of the broad-scale slope of the standing wave, as illustrated in Appendix B.

As discussed in Sect. 4.1, all the OH emission lines with $v_{\text{helio}} \lesssim 54\,400 \text{ km s}^{-1}$ stem from the 1667 MHz OH megamasers, and we hence adopted $b_i = 1.964 \text{ Hz } \mu\text{G}^{-1}$ in the fitting. As discussed above, the 1667 and 1665 MHz OH emission lines are likely mixed for the emission feature near $v_{\text{helio}} \sim 54\,725 \text{ km s}^{-1}$. For the velocity range $v_{\text{helio}} \sim 54\,400\text{--}54\,700 \text{ km s}^{-1}$, the 1667 and 1665 MHz lines might also be mixed, although observational support remains insufficient for two reasons: (1) as shown in the upper panel of Fig. 5, no obvious 1665 MHz emissions are detected in the range $v_{\text{helio}} \sim 54\,800\text{--}55\,100 \text{ km s}^{-1}$, and (2) the intensity ratio of the 1665 MHz to 1667 MHz lines in $v_{\text{helio}} \sim 54\,100\text{--}54\,200 \text{ km s}^{-1}$ is not anomalous. At least two possibilities exist: (1) the OH emissions in $v_{\text{helio}} \sim 54\,400\text{--}54\,700 \text{ km s}^{-1}$ are dominated by the 1665 MHz transition, or (2) these emissions are primarily from the 1667 MHz transition, but lack counterparts of 1665 MHz emissions at similar velocities. Based on the available FAST single-dish data, it remains challenging to distinguish between these scenarios. If the emissions in the velocity range $v_{\text{helio}} \sim 54\,400\text{--}54\,725 \text{ km s}^{-1}$ result from a combination of the 1665 MHz and 1667 MHz lines, the magnetic field fitting will involve derivatives of the Stokes I emission with uncertain contributions from each line, leading to a complex error propagation. For simplicity, we first adopted $b_i = 3.270 \text{ Hz } \mu\text{G}^{-1}$ for OH emission lines with $v_{\text{helio}} > 54\,400 \text{ km s}^{-1}$, and we then used $b_i = 1.964 \text{ Hz } \mu\text{G}^{-1}$ to repeat the fitting for further discussion.

In the following, we apply two methods to fit the observed I and V spectra. The first method follows the procedures described by Robishaw et al. (2008) and McBride & Heiles (2013) and first decomposes the I spectrum into multiple Gaussians and then examines the possible Zeeman splittings. The second method is to fit the I and V spectra simultaneously with multiple Gaussian components.

4.2.1. Fitting using the first method

Following the method described by Robishaw (2008) and McBride & Heiles (2013), we began by solving equation (4) by decomposing the Stokes I spectrum into multiple Gaussian components. Using the 18 Gaussian components given by McBride & Heiles (2013) as initial guesses, we identified five additional Gaussian components required to fit the features revealed by FAST observations. These include two emission line components near $v_{\text{helio}} \sim 55\,140 \text{ km s}^{-1}$ and $\sim 53\,580 \text{ km s}^{-1}$, one narrow emission line near $v_{\text{helio}} \sim 54\,327 \text{ km s}^{-1}$, and two components for resolved peaks around $v_{\text{helio}} \sim 54\,180 \text{ km s}^{-1}$ in the Stokes I spectrum. The fitting result of Stokes I is shown in the upper panel of Fig. 6. Then, these Gaussian components were used to derive $dI/d\nu$ to fit the V spectrum (e.g., Robishaw et al.

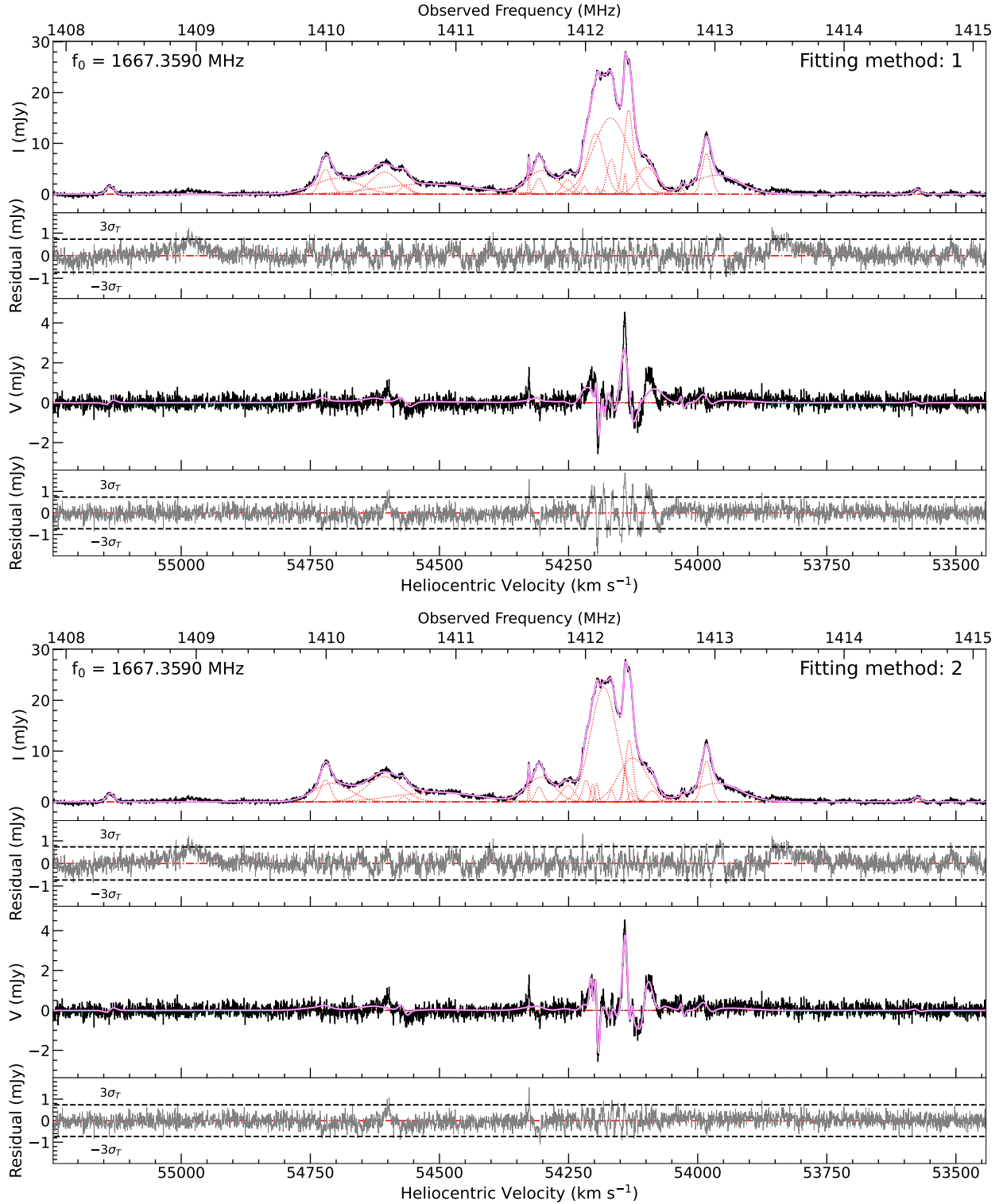


Fig. 6. Zeeman-splitting analysis of OH megamaser lines from IRAS 02524+2046. *Upper panels:* Stokes I and V spectral fits obtained using the method described in Sect. 4.2.1 (fitting method 1), while the *lower panels* display results from another approach in Sect. 4.2.2 (fitting method 2). For heliocentric velocity calculations, we adopted a rest frequency of $\nu_0 = 1667.3590$ MHz, although some spectral features originate from the 1665.4018 MHz OH transition.

2008; McBride & Heiles 2013), as presented in Fig. 6. The corresponding parameters are listed in Table 2.

Consistent with McBride & Heiles (2013), we obtained satisfactory fits for the Stokes I spectrum of OH megamasers in IRAS 02524+2046, but encountered difficulties in fitting the complex V profile features. Significant resid-

uals ($>3\sigma_T$, see Fig. 6) persist in the velocity range $v_{\text{helio}} \sim 54\,050\text{--}54\,250$ km s $^{-1}$, despite attempts to optimize initial guesses for a simultaneous I and V spectrum fitting. McBride & Heiles (2013) reported confident magnetic field detections (+12.27 to +23.88 mG) for five narrow components (Gaussians 3, 8, 9, 12, and 13 in their Table 7). We reproduced

Table 2. Zeeman-splitting analysis results obtained from fitting the Stokes I and V spectra of OH megamasers in IRAS 02524+2046 with the method described in Sect. 4.2.1.

Gaussian (1)	S (mJy) (2)	ν (MHz) (3)	$\Delta\nu$ (MHz) (4)	$B_{//}$ (mG) (5)	$B_{//}^{1st}$ (mG) (6)	$B_{//}^{2nd}$ (mG) (7)	Heliocentric velocity (km s $^{-1}$) (8)
1	1.65 ± 0.08	1408.3385 ± 0.0016	0.0299 ± 0.0016				54720.96 ± 0.40 [†]
2	4.88 ± 0.12	1409.9954 ± 0.0007	0.0436 ± 0.0011				54304.36 ± 0.18 [†]
3	3.14 ± 0.16	1410.0873 ± 0.0101	0.1700 ± 0.0077				54281.29 ± 2.55 [†]
4	4.35 ± 0.18	1410.4488 ± 0.0032	0.1058 ± 0.0055	3.6 ± 0.9*	1.8 ± 1.0*	5.5 ± 1.1*	54190.54 ± 0.81 [†]
5	1.65 ± 0.16	1410.6081 ± 0.0024	0.0400 ± 0.0035	6.5 ± 1.3*	5.8 ± 1.7*	7.5 ± 1.6*	54150.56 ± 0.60 [†]
6	2.02 ± 0.04	1410.7831 ± 0.0299	0.3664 ± 0.0243				54106.66 ± 7.51 [†]
7	3.97 ± 0.19	1411.5623 ± 0.0003	0.0054 ± 0.0003				54326.98 ± 0.07
8	3.12 ± 0.20	1411.6399 ± 0.0010	0.0299 ± 0.0016				54307.52 ± 0.24
9	4.65 ± 0.18	1411.6620 ± 0.0035	0.1107 ± 0.0047				54301.97 ± 0.89
10	2.81 ± 0.44	1411.8626 ± 0.0037	0.0424 ± 0.0039				54251.67 ± 0.92
11	1.55 ± 0.30	1411.9924 ± 0.0018	0.0168 ± 0.0027				54219.12 ± 0.45
12	11.84 ± 3.51	1412.0781 ± 0.0063	0.0659 ± 0.0099	11.4 ± 0.5	11.7 ± 0.6	10.3 ± 0.6	54197.62 ± 1.59
13	1.36 ± 0.29	1412.0935 ± 0.0017	0.0094 ± 0.0023	16.0 ± 1.3	13.0 ± 1.2	26.8 ± 2.5	54193.76 ± 0.44
14	0.79 ± 0.39	1412.1386 ± 0.0033	0.0105 ± 0.0049	17.6 ± 2.4	7.4 ± 8.0	14.7 ± 2.8	54182.46 ± 0.84
15	14.99 ± 2.56	1412.1953 ± 0.0378	0.1349 ± 0.0181	-11.5 ± 0.5	-11.1 ± 0.8	-11.5 ± 0.6	54168.24 ± 9.47
16	6.81 ± 1.40	1412.1989 ± 0.0026	0.0335 ± 0.0032	9.2 ± 0.6	10.4 ± 0.9	8.0 ± 0.7	54167.35 ± 0.64
17	3.95 ± 0.29	1412.3056 ± 0.0004	0.0091 ± 0.0007				54140.62 ± 0.10
18	16.52 ± 1.51	1412.3329 ± 0.0013	0.0354 ± 0.0015	6.8 ± 0.2	6.3 ± 0.3	7.0 ± 0.3	54133.77 ± 0.32
19	5.30 ± 1.59	1412.4760 ± 0.0155	0.0733 ± 0.0078	-13.4 ± 1.1	-11.5 ± 1.3	-14.6 ± 1.3	54097.91 ± 3.89
20	1.01 ± 0.12	1412.7497 ± 0.0017	0.0130 ± 0.0019	7.7 ± 2.0	9.5 ± 2.4	5.6 ± 2.4	54029.34 ± 0.43
21	7.97 ± 0.08	1412.9354 ± 0.0004	0.0358 ± 0.0005	2.1 ± 0.4	1.9 ± 0.5	2.2 ± 0.5	53982.86 ± 0.10
22	3.73 ± 0.05	1413.0107 ± 0.0024	0.1782 ± 0.0022				53964.01 ± 0.61
23	0.98 ± 0.08	1414.5672 ± 0.0026	0.0277 ± 0.0026				53574.74 ± 0.64

Notes. Column (1) numbers the Gaussian components. Columns (2)–(4) present the fit parameters (peak flux density, line center, and line width) with their 1σ uncertainties. Column (5) shows the derived magnetic field strength and its uncertainty, where values annotated with an asterisk designate components attributed to the 1665 MHz OH transition (using a splitting coefficient of 3.270 Hz μG^{-1}). When these emissions are instead assumed to be dominated by 1667 MHz OH transition using a splitting coefficient of 1.964 Hz μG^{-1} , the derived values are 6.1 ± 1.5 mG and 10.9 ± 2.2 mG for Gaussian components 4 and 5, respectively. Columns (6) and (7) separately list magnetic field values obtained from fitting the first- and second-epoch observations independently. Column (8) gives the heliocentric velocities, and the dagger denotes values corresponding to the assumed 1665 MHz OH maser components.

four of these components, but did not detect their Gaussian component 13 because the local peak at 1412.5320 MHz observed by McBride & Heiles (2013) is absent in our FAST spectra. Our magnetic field measurements agree with theirs within 3σ uncertainties for components 3, 8, and 9 in their Table 7. However, for their component 12 ($B_{//} = 13.65 \pm 1.07$ mG in McBride & Heiles 2013), we measure a smaller field (6.8 ± 0.2 mG, i.e., our component 18 in Table 2). The discrepancy in the fitting results for this component is likely attributable to the intrinsic variability of the magnetic field. Moreover, these findings support a predominantly positive orientation of the magnetic field within the OH megamasers of IRAS 02524+2046.

4.2.2. Fitting using the second method

An optimal decomposition of multiple OH megamaser components should accurately reproduce the I spectrum and detailed V spectrum features. To achieve this, we improved the initial fitting method by simultaneously fitting the I and V spectra with additional Gaussian components, which significantly reduced the residuals present in previous approaches. For model selection, we employed the Akaike information criterion (AIC, Akaike 1974) and Bayesian information criterion (BIC, Schwarz 1978) to balance the goodness-of-fit against the model complexity. The

AIC is calculated as $N \ln(\sum (y_i^{\text{model}} - y_i^{\text{obs}})^2 / N) + 2k$, and the BIC = $N \ln(\sum (y_i^{\text{model}} - y_i^{\text{obs}})^2 / N) + k \ln(N)$, where N represents the number of spectral channels, k is the number of free parameters, and y_i^{model} and y_i^{obs} denote the modeled and observed flux densities in the i th channel respectively. These criteria enabled us to fit spectral features above $3\sigma_T$ significance (see Fig. 6) while minimizing the number of Gaussian components required to achieve reasonable residuals.

The lower panel of Fig. 6 shows that the final model incorporates 25 Gaussian components and successfully reproduces the I and V spectra. The corresponding parameters are listed in Table 3. To estimate the parameter uncertainties, we employed a bootstrap resampling approach by separating the IRAS 02524+2046 observational data into 110 files, each of which contained the observational results of one minute on-source integration. We generated 1000 bootstrap samples for the I and V spectra by random resampling. The fitting results of the 1000 samples were used to calculate parameter errors.

Compared to the first method, our analysis reveals two additional Gaussian components in the velocity range $v_{\text{helio}} \sim 54\,050\text{--}54\,250$ km s $^{-1}$, corresponding to complex features in the I and V profiles. We detect significant magnetic fields ($>3\sigma$) for ten components: eight components from the 1667 MHz transition, and two components from the assumed 1665 MHz line

Table 3. Same as Table 2: Analysis results obtained using the method described in Sect. 4.2.2.

Gaussian (1)	S (mJy) (2)	ν (MHz) (3)	$\Delta\nu$ (MHz) (4)	$B_{//}$ (mG) (5)	$B_{//}^{1st}$ (mG) (6)	$B_{//}^{2nd}$ (mG) (7)	Heliocentric velocity (km s ⁻¹) (8)
1	1.65 ± 0.07	1408.3387 ± 0.0014	0.0298 ± 0.0014				54720.91 ± 0.35 [†]
2	4.35 ± 0.11	1409.9958 ± 0.0007	0.0388 ± 0.0010				54304.28 ± 0.17 [†]
3	3.68 ± 0.10	1410.0460 ± 0.0046	0.1406 ± 0.0042				54291.67 ± 1.16 [†]
4	4.99 ± 0.20	1410.4444 ± 0.0027	0.1361 ± 0.0046	4.0 ± 0.8*	2.8 ± 1.0*	5.7 ± 1.1*	54191.66 ± 0.67 [†]
5	1.04 ± 0.09	1410.6005 ± 0.0020	0.0264 ± 0.0025	7.3 ± 1.7*	7.8 ± 2.4*	7.0 ± 1.9*	54152.48 ± 0.50 [†]
6	1.90 ± 0.04	1410.8472 ± 0.0280	0.3175 ± 0.0217				54090.58 ± 7.03 [†]
7	3.94 ± 0.17	1411.5624 ± 0.0002	0.0051 ± 0.0003				54326.96 ± 0.06
8	2.93 ± 0.17	1411.6410 ± 0.0009	0.0290 ± 0.0015				54307.25 ± 0.24
9	4.85 ± 0.16	1411.6553 ± 0.0028	0.1068 ± 0.0038				54303.65 ± 0.69
10	3.22 ± 0.16	1411.8640 ± 0.0026	0.0495 ± 0.0027				54251.30 ± 0.65
11	4.23 ± 0.39	1412.0049 ± 0.0010	0.0266 ± 0.0017				54215.97 ± 0.25
12	3.40 ± 0.21	1412.0550 ± 0.0009	0.0144 ± 0.0009	11.7 ± 1.0	14.6 ± 1.5	11.0 ± 1.2	54203.43 ± 0.23
13	3.62 ± 0.26	1412.0870 ± 0.0006	0.0130 ± 0.0005	17.1 ± 1.2	14.9 ± 1.2	20.0 ± 2.0	54195.39 ± 0.15
14	22.56 ± 0.29	1412.1406 ± 0.0027	0.1008 ± 0.0026				54181.96 ± 0.69
15	2.43 ± 0.15	1412.2011 ± 0.0008	0.0165 ± 0.0010	-4.4 ± 0.9	-6.1 ± 1.4	-3.5 ± 1.1	54166.80 ± 0.20
16	6.89 ± 0.54	1412.3052 ± 0.0006	0.0134 ± 0.0006				54140.70 ± 0.15
17	12.18 ± 0.84	1412.3370 ± 0.0010	0.0292 ± 0.0006	18.4 ± 2.1	19.5 ± 4.6	17.0 ± 1.5	54132.74 ± 0.25
18	1.83 ± 0.71	1412.3473 ± 0.0010	0.0155 ± 0.0013				54130.16 ± 0.24
19	8.63 ± 0.83	1412.3662 ± 0.0058	0.1116 ± 0.0024	-24.5 ± 3.8	-21.1 ± 3.3	-32.8 ± 9.1	54125.42 ± 1.45
20	0.39 ± 0.51	1412.3964 ± 0.0020	0.0329 ± 0.0023				54117.85 ± 0.49
21	2.20 ± 0.21	1412.5148 ± 0.0031	0.0398 ± 0.0030	20.6 ± 3.2	16.5 ± 3.0	29.8 ± 6.3	54088.20 ± 0.77
22	0.87 ± 0.11	1412.7501 ± 0.0014	0.0119 ± 0.0014	8.4 ± 2.4	11.9 ± 3.7	5.8 ± 2.5	54029.24 ± 0.34
23	8.02 ± 0.07	1412.9356 ± 0.0003	0.0362 ± 0.0004	2.0 ± 0.4	1.9 ± 0.5	2.2 ± 0.5	53982.81 ± 0.09
24	3.64 ± 0.04	1413.0112 ± 0.0022	0.1838 ± 0.0021				53963.86 ± 0.56
25	0.98 ± 0.07	1414.5674 ± 0.0023	0.0277 ± 0.0023				53574.70 ± 0.57

Notes. Same as the notes of Table 2. In Column (5), the values annotated with an asterisk designate components attributed to the 1665 MHz OH transition. When these emissions are instead assumed to be dominated by the 1667 MHz OH transition, the derived values are 6.6 ± 1.3 mG and 12.1 ± 2.8 mG.

as given in Table 3. The measured field strengths range from -24.5 mG to $+20.6$ mG, with a predominance of positive values (8/10 cases). To verify these results, we independently analyzed data from both observational epochs and found consistent magnetic field measurements within 3σ uncertainties, as tabulated in Table 3. For four of the five components with previously reported confident detections by McBride & Heiles (2013), their Gaussians 3, 8, 12, and 13), our measurements agree within 3σ uncertainties. However, we obtained negative field values for the remaining one component, where McBride & Heiles (2013) reported positive fields. Based on earlier findings, the emissions in the velocity range $v_{\text{helio}} \sim 54\,400\text{--}54\,725$ km s⁻¹ likely represent a blend of the 1665 MHz and 1667 MHz OH lines. We therefore reapplied the fitting procedure by adopting a splitting coefficient $b_i = 1.964$ Hz μG^{-1} . With the exception of Gaussian components 4 and 5, the derived magnetic fields are consistent with the values reported in Table 3. Specifically, the best-fit solutions for components 4 and 5 yield larger magnetic field strengths and associated uncertainties: 6.6 ± 1.3 mG and 12.1 ± 2.8 mG, respectively.

In the fitting results of Stokes V spectra (Fig. 6), the narrow emission line near $v_{\text{helio}} \sim 54\,327$ km s⁻¹ cannot be well fit by the above methods, warranting further observational investigation. The narrow emission line shows a velocity offset of about 0.5 km s⁻¹ between its Stokes I peak ($v_{\text{helio}} \sim 54\,326.96$ km s⁻¹) and Stokes V peak ($v_{\text{helio}} \sim 54\,326.42$ km s⁻¹), with a line width of approximately 2.6 km s⁻¹ in the Stokes I spectrum. One possible explanation is that it corresponds to one component of a

Zeeman pair whose LCP and RCP components are split by an interval larger than the line width, and only the stronger component is detected. As observed in Galactic OH masers (e.g., Green et al. 2015), the ratios of the peak flux densities between the LCP and RCP components for Zeeman pairs can range from 0.3 to 2.4.

5. Discussions and conclusions

We developed polarization calibration procedures for L -band spectral observations and applied them to FAST data of the OH megamaser galaxy IRAS 02524+2046. Through complete Mueller matrix solutions, we achieved a circular polarization calibration with an accuracy of $\sim 0.01\%$ – 0.08% across the 1050–1450 MHz frequency range. We also emphasize that regular calibrator observations are necessary to maintain the polarization calibration accuracy.

The FAST observations of IRAS 02524+2046 revealed detailed OH megamaser features in the Stokes I spectrum, including a narrow emission line component with a line width of 2.6 km s⁻¹, two emission line components showing large velocity shifts from the systemic galaxy velocity, and multiple OH emission peaks resolved by the high-spectral resolution. In addition, a narrow emission line feature near the expected frequency of the redshifted 1720 MHz OH line was detected, making IRAS 02524+2046 a new galaxy with a detected OH satellite line.

The detection of the 1665 MHz OH megamaser feature at the heliocentric velocity $\sim 54\,725\text{ km s}^{-1}$ is particularly significant and suggests that the previously observed unusual flux ratio of the pair of 1665 and 1667 MHz OH megamasers likely results from blended emission of both transitions at similar observed frequencies. Our analysis revealed that the 1667 MHz OH megamaser emission lines in IRAS 02524+2046 spans an exceptionally wide velocity range from $v_{\text{helio}} \sim 54\,750$ to $\sim 53\,580\text{ km s}^{-1}$, indicating greater complexity than previously recognized. These observations imply that some maser-emitting clumps exhibit large velocity offsets from the systemic galaxy velocity, which is intriguing for OH megamaser galaxies (e.g., Harvey-Smith et al. 2016). Possible explanations include outflows driven by active galactic nuclei, nuclear starbursts, combined effects of active galactic nuclei and starbursts (e.g., González-Alfonso et al. 2017), an association with dual galactic nuclei, or a molecular ring orbiting a supermassive black hole (e.g., Harvey-Smith et al. 2016).

The sensitive polarization observations by FAST reveal detailed local features in the Stokes V profiles of the 1665 and 1667 MHz OH megamasers from IRAS 02524+2046, including distinct peaks and dips. We simultaneously fit the I and V spectra to decompose the OH megamaser emissions into multiple Gaussian components, identifying ten components with significant Zeeman splitting ($>3\sigma$). The derived magnetic field strengths span -24.5 mG to $+20.6\text{ mG}$, with eight components showing positive values.

The case study of IRAS 02524+2046 demonstrated that sensitive polarization observations with a high spectral resolution are essential for resolving individual maser components and their Zeeman splitting features. These results also indicate that magnetic field measurements derived from some of the individual Gaussian components in single-dish observations require careful interpretation. The overall preferential magnetic field orientation of a galaxy likely provides more reliable physical insight, although high angular resolution very long baseline observations may ultimately be needed to reliably measure the characteristics of the magnetic fields traced by OH megamasers.

Acknowledgements. We thank the anonymous referee for the very careful reading and helpful suggestions. This work is supported by the National SKA Program of China (Grant No. 2022SKA0120103) and the National Natural Science Foundation of China (Grant No. 12588202 and 11933011). XYG and JLH are additionally supported by the International Partnership Program of Chinese Academy of Sciences, Grant No. 114A11KYSB20170044. TH thanks the support from the Youth Innovation Promotion Association CAS. LGH thanks for the helpful discussions with Dr. W.C. Jing for the polarization calibration, and Dr. J. Xu for correcting the influence of the Earth's ionosphere on the calibration results. This work made use of the data from FAST (Five-hundred-meter Aperture Spherical radio Telescope) (<https://cstr.cn/31116.02.FAST>). FAST is a Chinese national mega-science facility, operated by the National Astronomical Observatories, Chinese Academy of Sciences.

References

- Akaike, H. 1974, *IEEE Trans. Autom. Control*, 19, 716
 Baan, W. A., & Haschick, A. D. 1987, *ApJ*, 318, 139
 Baan, W. A., Haschick, A. D., & Henkel, C. 1989, *ApJ*, 346, 680
 Baan, W. A., Haschick, A., & Henkel, C. 1992, *AJ*, 103, 728
 Caswell, J. L., Green, J. A., & Phillips, C. J. 2013, *MNRAS*, 431, 1180
 Caswell, J. L., Green, J. A., & Phillips, C. J. 2014, *MNRAS*, 439, 1680
 Chen, X., Ching, T.-C., Li, D., et al. 2025, *AJ*, 169, 158
 Ching, T. C., Li, D., Heiles, C., et al. 2022, *Nature*, 601, 49
 Ching, T.-C., Heiles, C., Li, D., et al. 2025, *AJ*, 170, 116
 Darling, J. 2005, *ASP Conf. Ser.*, 340, 216
 Darling, J. 2007, *IAU Symp.*, 242, 417
 Darling, J., & Giovanelli, R. 2000, *AJ*, 119, 3003
 Darling, J., & Giovanelli, R. 2001, *AJ*, 121, 1278
 Darling, J., & Giovanelli, R. 2002a, *AJ*, 124, 100
 Darling, J., & Giovanelli, R. 2002b, *ApJ*, 569, L87
 Darling, J., & Giovanelli, R. 2002c, *ApJ*, 572, 810
 Darling, J., & Giovanelli, R. 2006, *AJ*, 132, 2596
 Gao, X., Reich, W., Sun, X., et al. 2022, *Sci. China Phys. Mech. Astron.*, 65, 129705
 González-Alfonso, E., Fischer, J., Spoon, H. W. W., et al. 2017, *ApJ*, 836, 11
 Green, J. A., Caswell, J. L., & McClure-Griffiths, N. M. 2015, *MNRAS*, 451, 74
 Han, J. L., Wang, C., Wang, P. F., et al. 2021, *RAA*, 21, 107
 Harvey-Smith, L., Allison, J. R., Green, J. A., et al. 2016, *MNRAS*, 460, 2180
 Heiles, C., Goodman, A. A., McKee, C. F., & Zweibel, E. G. 1993, in *Protostars and Planets III*, eds. E. H. Levy, & J. I. Lunine, 279
 Heiles, C., Perillat, P., Nolan, M., et al. 2001, *PASP*, 113, 1274
 Hong, T., Han, J., Hou, L., et al. 2022, *Sci. China Phys. Mech. Astron.*, 65, 129702
 Hou, L., Han, J., Hong, T., Gao, X., & Wang, C. 2022, *Sci. China Phys. Mech. Astron.*, 65, 129703
 Jiang, P., Tang, N.-Y., Hou, L.-G., et al. 2020, *RAA*, 20, 064
 Jing, W. C., Han, J. L., Hong, T., et al. 2023, *MNRAS*, 523, 4949
 Lockett, P., & Elitzur, M. 2008, *ApJ*, 677, 985
 McBride, J., & Heiles, C. 2013, *ApJ*, 763, 8
 McBride, J., Heiles, C., & Elitzur, M. 2013, *ApJ*, 774, 35
 McBride, J., Robishaw, T., Heiles, C., Bower, G. C., & Sarma, A. P. 2015, *MNRAS*, 447, 1103
 Nan, R. 2006, *Sci. China Phys. Mech. Astron.*, 49, 129
 Nedoluha, G. E., & Watson, W. D. 1990, *ApJ*, 361, 653
 Peng, H., Wu, Z., Zhang, B., et al. 2020, *A&A*, 638, A78
 Robishaw, T. 2008, Ph.D. Thesis, University of California, Berkeley
 Robishaw, T., & Heiles, C. 2021, in *The WSPC Handbook of Astronomical Instrumentation, Volume 1: Radio Astronomical Instrumentation*, ed. A. Wolszczan, 127
 Robishaw, T., Quataert, E., & Heiles, C. 2008, *ApJ*, 680, 981
 Schwarz, G. 1978, *Ann. Stat.*, 6, 461
 Sotomayor-Beltran, C., Sobey, C., Hessels, J. W. T., et al. 2013, *A&A*, 552, A58
 Sun, X.-H., Meng, M.-N., Gao, X.-Y., et al. 2021, *RAA*, 21, 282
 Taylor, A. R., & Legodi, L. S. 2024, *AJ*, 167, 273
 Wang, P. F., Han, J. L., Xu, J., et al. 2023, *RAA*, 23, 104002
 Wang, T., Wang, C., Han, J. L., et al. 2024, *MNRAS*, 528, 2501
 Watson, W. D. 2009, *Rev. Mexicana Astron. Astrofis. Conf. Ser.*, 36, 113
 Wu, Z., Sotnikova, Y. V., Zhang, B., et al. 2023, *A&A*, 669, A148
 Xiao, L., Zhu, M., Sun, X.-H., Jiang, P., & Sun, C. 2023, *ApJ*, 952, 94
 Xu, J., Han, J., Wang, P., & Yan, Y. 2022, *Sci. China Phys. Mech. Astron.*, 65, 129704
 Zhou, D. J., Han, J. L., Jing, W. C., et al. 2023a, *MNRAS*, 526, 2657
 Zhou, D. J., Han, J. L., Xu, J., et al. 2023b, *RAA*, 23, 104001

Appendix A: Parameters of Mueller matrix for the central beam

The fitted values and their associated uncertainties for the five Mueller matrix parameters (ΔG , ψ , ϵ , ϕ , and α) are summarized in the corresponding panels in Fig. A.1 for the 1050–1150 MHz and 1300–1450 MHz frequency bands. As discussed in Ching et al. (2025), the parallactic angle θ and the parameter α are coupled in the solution of the Mueller matrix. A small systematic error in θ may propagate to the fitted α values. In the lower panel of Fig. A.1, the nearly constant fitted α values across different frequencies likely indicate a systematic error in θ originating from imperfections in the mechanical control of the receiver rotation.

Appendix B: Baseline and standing wave removal in spectral data processing

We employ a modified sinusoidal function (Jing et al. 2023) combined with third-order polynomials to model and remove standing waves and spectral baselines. Fig. B.1 and B.2 demonstrate this technique through two applications: (1) Galactic HI 21 cm lines toward *IRAS* 02524+2046 (Galactic coordinates $l = 158.0^\circ$, $b = -33.3^\circ$), and (2) OH megamasers in *IRAS* 02524+2046.

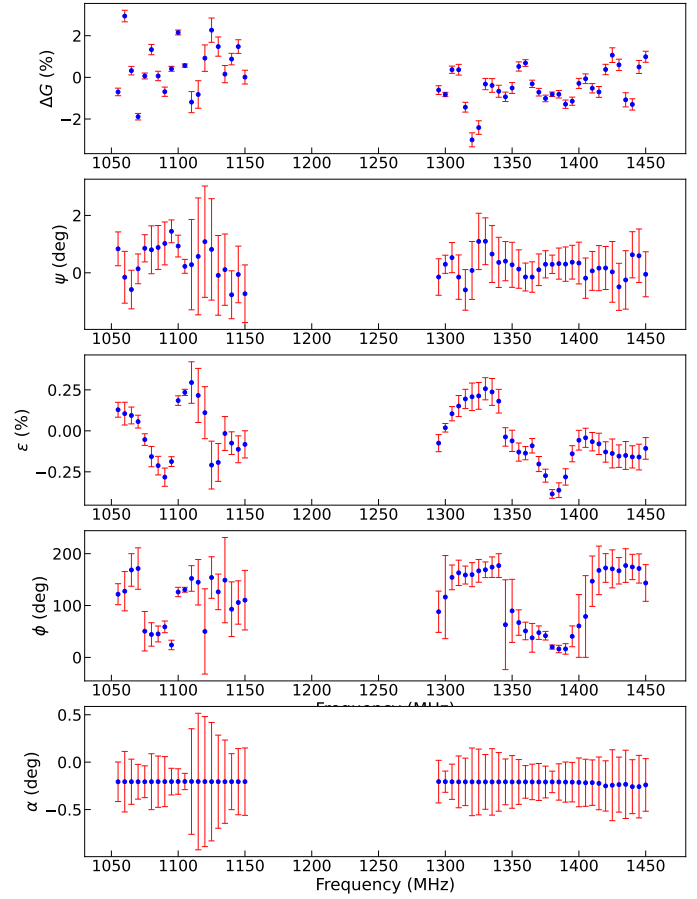


Fig. A.1. Frequency dependence of the five fitted Mueller matrix parameters (ΔG , ψ , ϵ , ϕ , and α) across the 1050–1150 MHz and 1300–1450 MHz bands. Data are derived from FAST observations of 3C 286 on 19 August 2023.

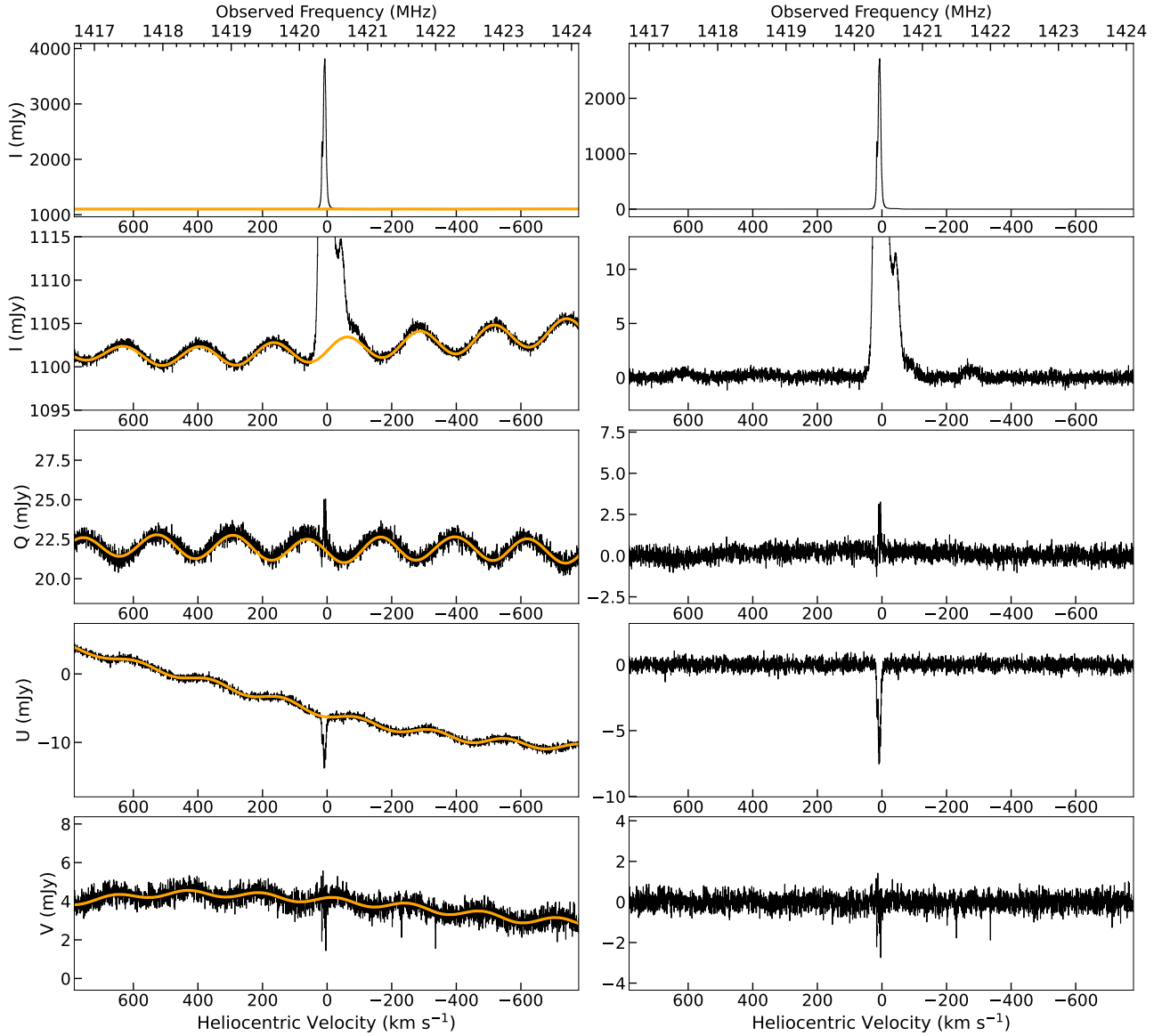


Fig. B.1. *Left panels* show the Stokes I , Q , U , and V spectra (black) of Galactic HI 21 cm emission toward *IRAS* 02524+2046 ($l = 158.0^\circ$, $b = -33.3^\circ$) observed by FAST on 12 August 2023, with orange curves indicating the fitted baseline and standing wave models. The *right panels* present the spectra after subtracting these components.

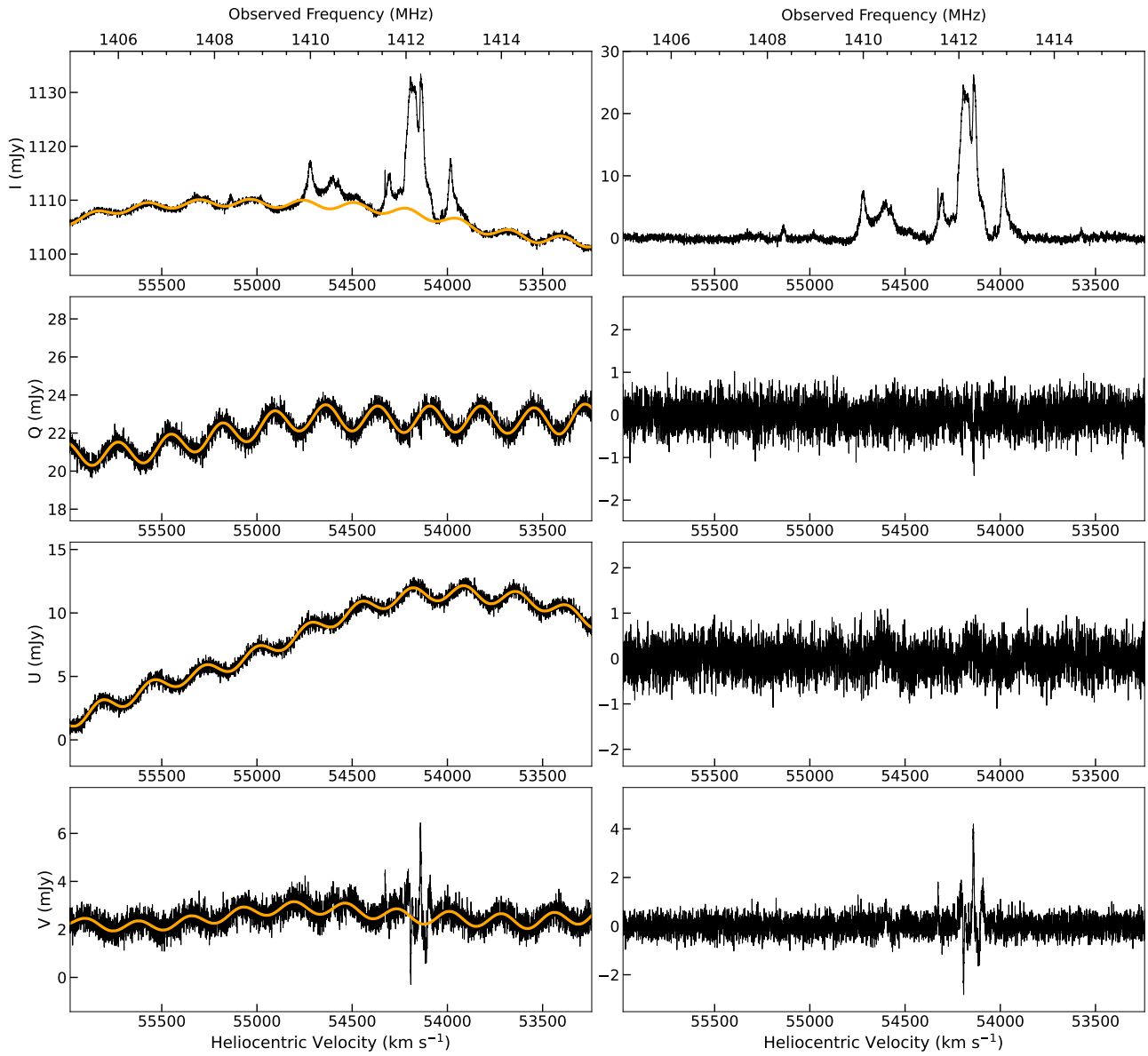


Fig. B.2. Same format as Fig. B.1, showing the results for the 1665 MHz and 1667 MHz OH megamaser emission from *IRAS* 02524+2046 observed by FAST on 12 August 2023.